European Journal of Mechanics B/Fluids 28 (2009) 578–589

Contents lists available at ScienceDirect

European Journal of Mechanics B/Fluids

www.elsevier.com/locate/ejmflu

Turbulence statistics and energy budget in rotating Rayleigh–Bénard convection

R.P.J. Kunnen [a,*,1], B.J. Geurts [b,a], H.J.H. Clercx [a,b]

[a] Fluid Dynamics Laboratory, Department of Physics, International Collaboration for Turbulence Research (ICTR) & J.M. Burgers Centre for Fluid Dynamics, Eindhoven University of Technology, P.O. Box 513, 5600 MB Eindhoven, The Netherlands

[b] Department of Applied Mathematics, International Collaboration for Turbulence Research (ICTR) & J.M. Burgers Centre for Fluid Dynamics, University of Twente, P.O. Box 217, 7500 AE Enschede, The Netherlands

ARTICLE INFO

Article history:
Received 28 August 2008
Received in revised form 16 January 2009
Accepted 28 January 2009
Available online 3 February 2009

Keywords:
Rotating Rayleigh–Bénard convection
Turbulence
Direct numerical simulation
Energy budget

ABSTRACT

The strongly-modified turbulence statistics of Rayleigh–Bénard convection subject to various rotation rates is addressed by numerical investigations. The flow is simulated in a domain with periodic boundary conditions in the horizontal directions, and confined vertically by parallel no-slip isothermal walls at the bottom and top. Steady rotation is applied about the vertical. The rotation rate, or equivalently the Rossby number Ro, is varied such that Ro ranges from ∞ (no rotation) to $Ro = 0.1$ (strong rotation). Two different Rayleigh numbers are used, viz. $Ra = 2.5 \times 10^6$ and 2.5×10^7, characterising buoyancy due to temperature differences. The Prandtl number $\sigma = 1$, close to the value for air. Horizontally averaged statistics show that rotation reduces the turbulence intensity, although probability density functions clearly show that considerable (preferably cyclonic) vorticity is added to the flow by the Ekman boundary layers on the solid walls. Rotation changes the balance of the turbulent kinetic energy budget. It is found that for a range of rotation rates the buoyant production is higher than without rotation. Therefore, at appropriate rotation rates the heat flux through the fluid layer is increased relative to the non-rotating case. At sufficiently rapid rotation, however, the heat flux through the fluid layer is strongly attenuated.

1. Introduction

Large-scale fluid flows on Earth are primarily driven by convection and shaped by the Coriolis force due to the planetary rotation. A striking example is the occurrence of deep convective chimneys in polar seas, see for example Refs. [1–3]. This extends to many other celestial bodies. For example, the outer layer of our Sun is known to be very convective, with strong influences coming from the axial rotation of the Sun; for a review see Miesch [4]. Further examples are the giant planets in our solar system (see, e.g., Busse [5] and references therein). Thus, next to its fundamental interest, rotating convection is a topic with broad relevance for geophysics and astrophysics.

A relatively simple model for these complex flows is found in Rayleigh–Bénard convection [6–8], augmented with a background rotation (see, e.g., Sprague et al. [9] and references therein). The Rayleigh–Bénard flow problem is defined by an unbounded horizontal layer of fluid confined vertically by parallel walls and heated from below. Rayleigh–Bénard convection is governed by two dimensionless groups; the Rayleigh number Ra and the Prandtl number σ:

$$Ra \equiv \frac{g\alpha \Delta T H^3}{\nu\kappa}, \qquad \sigma \equiv \frac{\nu}{\kappa}, \tag{1}$$

with g the gravitational acceleration pointing downward, and H and ΔT the vertical separation and temperature difference between the walls, respectively. The fluid has kinematic viscosity ν, thermal diffusivity κ, and thermal expansion coefficient α. The Rayleigh number characterises the importance of buoyancy relative to diffusion in the flow. The Prandtl number describes the diffusive properties of the fluid.

To describe the effects of rotation an additional parameter is needed, the Taylor number Ta:

$$Ta \equiv \left(\frac{2\Omega H^2}{\nu}\right)^2. \tag{2}$$

Here Ω is the rotation rate, assumed to point counter to the gravitational acceleration in the current study. A very useful combination of these three dimensionless numbers is found when inserting the so-called free-fall velocity $U \equiv \sqrt{g\alpha \Delta T H}$ [10,11] in the so-called Rossby number $Ro = U/(2\Omega H)$. This results in:

$$Ro \equiv \sqrt{\frac{Ra}{\sigma\, Ta}} \tag{3}$$

which quantifies the relative importance of buoyancy and rotation in rotating Rayleigh–Bénard flow.

* Corresponding author.
E-mail address: r.kunnen@aia.rwth-aachen.de (R.P.J. Kunnen).
[1] Present address: Institute of Aerodynamics, RWTH Aachen University, Wüllnerstraße 5a, 52062 Aachen, Germany. Tel.: +49 241 809 0419; fax: +49 241 809 2257.

0997-7546/$ – see front matter
doi:10.1016/j.euromechflu.2009.01.003

In the absence of rotation Lord Rayleigh's well-known classical result [12] identifies a critical Rayleigh number $Ra_c = 1708$ for the onset of convection as transport mechanism next to conduction. With rotation the Ra_c dependence on rotation (Chandrasekhar [13,14])

$$Ra_c \simeq 8.7 Ta^{2/3}, \tag{4}$$

is valid for $Ta \gtrsim 10^4$. Rotation thus stabilises the fluid layer, i.e., the onset of convection is delayed, occurring at higher Ra. Nevertheless, at any given Ta, sufficiently large values of Ra will yield a fully developed turbulent flow.

An important problem in many studies on rotating convection is the heat transfer through the fluid layer as a function of the parameters mentioned above [15–23]. This heat transfer is commonly expressed by the Nusselt number Nu, defined as the heat-current density q divided by the conductive flux in absence of fluid motion:

$$Nu \equiv \frac{qH}{\lambda \Delta T}, \tag{5}$$

where λ is the thermal conductivity for the still fluid. In non-rotating convection only recently a theory has been developed that divides the dependence of Nu on Ra and σ into several phases using a modified boundary-layer theory [7,24,25]. With rotation, however, such a description is still lacking.

The early experiments by Rossby [15] showed that the addition of a modest rotation *increases* the Nusselt number compared to the non-rotating value. This is counter-intuitive when taking into account the stabilising effect of rotation [13,14], and can be interpreted in terms of rotation effects in boundary layers near the container walls. The observation of increased heat flux under rotation was verified in other experiments [18,19] and simulations [22,23,26].

It is generally accepted that the so-called Ekman pumping of viscous boundary layers under rotation [27] is the cause of the increase in Nu at sufficiently low rotation rates. We provide a quantitative view of this effect by analysing the kinetic energy budget of rotating convection for several rotation rates using direct numerical simulation (DNS). The energy budgets reveal that rotation causes larger buoyant production close to the walls. This is balanced by increased dissipation in the bulk region. Furthermore, we address changes in the flow statistics of convection due to application of various rotation rates. It is found that rotation attenuates turbulence intensities even when the total heat flux is increased. Rotation injects additional vorticity into the flow via the walls, where cyclonic vorticity is preferred.

We start with a description of the numerical method and the simulation procedure in Section 2. The presentation of the results is split into three parts: averaged vertical profiles of velocity, vorticity and temperature are discussed in Section 3.1, probability density functions of velocity, vorticity and temperature at two different vertical positions are shown in Section 3.2, and the kinetic energy balance is presented in Section 3.3. The conclusions are summarised in Section 4.

2. Numerical procedure and validation

The governing equations of turbulent rotating convection in horizontally unbounded domains are the incompressible Navier–Stokes and temperature equations, augmented with a rotation that is directed vertically anti-parallel to gravity. These equations are expressed in the Boussinesq approximation [14]:

$$\frac{\partial \mathbf{u}}{\partial t} + (\mathbf{u}\cdot\nabla)\mathbf{u} + \frac{1}{Ro}\hat{\mathbf{z}}\times\mathbf{u} = -\nabla p + \sqrt{\frac{\sigma}{Ra}}\nabla^2\mathbf{u} + T\hat{\mathbf{z}},$$

$$\frac{\partial T}{\partial t} + (\mathbf{u}\cdot\nabla)T = \frac{1}{\sqrt{\sigma Ra}}\nabla^2 T,$$

Table 1
Parameter values and resolution settings of the simulations. Note the increased vertical resolution for the four highest-Ta values at $Ra = 2.5\times10^6$; this is to resolve the viscous boundary layer whose thickness decreases considerably at high rotation rates.

	$Ra = 2.5\times10^6$		$Ra = 2.5\times10^7$	
Ro	Ta	$N_x\times N_y\times N_z$	Ta	$N_x\times N_y\times N_z$
∞	0	$128\times128\times64$	–	–
4.00	1.6×10^5	$128\times128\times64$	1.6×10^6	$192\times192\times128$
3.20	2.4×10^5	$128\times128\times64$	2.4×10^6	$192\times192\times128$
2.50	4.0×10^5	$128\times128\times64$	4.0×10^6	$192\times192\times128$
1.33	1.4×10^6	$128\times128\times64$	1.4×10^7	$192\times192\times128$
1.00	–	–	2.5×10^7	$192\times192\times128$
0.75	4.5×10^6	$128\times128\times64$	4.5×10^7	$192\times192\times128$
0.50	1.0×10^7	$128\times128\times64$	1.0×10^8	$192\times192\times128$
0.40	1.6×10^7	$128\times128\times64$	1.6×10^8	$192\times192\times128$
0.33	2.3×10^7	$128\times128\times64$	2.3×10^8	$192\times192\times128$
0.25	4.0×10^7	$128\times128\times128$	–	–
0.16	1.0×10^8	$128\times128\times128$	–	–
0.13	1.5×10^8	$128\times128\times128$	–	–
0.10[1]	2.5×10^8	$128\times128\times128$	–	–

[1] According to Chandrasekhar's stability criterion (4) this situation should remain stable: convection is completely suppressed, the linear temperature gradient persists and $Nu = 1$.

$$\nabla\cdot\mathbf{u} = 0. \tag{6}$$

Here $\mathbf{u}$ is the velocity vector, t stands for time, $\hat{\mathbf{z}}$ is the vertical unit vector, and p and T the pressure and temperature, respectively. These equations are written in dimensionless form; lengths are normalised with H and temperatures with ΔT. The time is scaled with the convective time scale $\tau \equiv H/U$ based on the free-fall velocity U introduced above. This time scale is considered more appropriate to the parameter regimes under study here than the diffusive time scale $\tau_\nu \equiv H^2/\nu$ (which is equal to $\tau_\kappa \equiv H^2/\kappa$ as $\sigma = 1$). The choice of a time scale that is independent of Ω simplifies the comparison of velocities and vorticities at various different rotation rates (equivalently: Rossby numbers), which is our prime aim in this article. The comparison between results at different Rayleigh numbers, however, is less direct since U scales as $Ra^{1/2}$ and correspondingly $\tau \sim Ra^{-1/2}$.

The equations are solved on a rectilinear domain with periodic boundary conditions in the horizontal directions. Both top and bottom walls are no-slip ($\mathbf{u} = \mathbf{0}$) and isothermal: $T = 0$ at the top wall ($z = 1$) and $T = 1$ on the bottom wall ($z = 0$). The horizontal extent of the domain is important, as it should not strongly influence the flow by imposing a length scale through the periodicity. The natural horizontal length scale should therefore be considerably smaller than the horizontal extent of the computational domain. Motivated by the fact that the horizontal scale decreases when rotation is applied [14,28] and the observation that the statistics of velocity and temperature at $Ta = 0$ are only significantly affected as the domain width becomes comparable to its height [29], the horizontal lengths are taken twice the vertical size. At the lowest non-zero Taylor number considered here, $Ta = 1.6\times10^5$ (Table 1), the critical wavenumber for onset of convection is $k_c H = 8.1$ [14], comparable to the minimal domain size constraints used by Julien et al. [10,30]. k_c is larger at higher Ta [14]; the horizontal length scale decreases when rotation is increased.

The discretisation of the equations follows the skew-symmetric scheme proposed by Verstappen and Veldman [31]. By adhering to the (skew-)symmetry of the original differential operators, stability of the scheme is ensured on any grid, as well as conservation of mass and momentum, and, for the inviscid case, energy conservation. Second-order accurate difference formulations combined with Richardson extrapolation give fourth-order accuracy in this approach, at sufficiently fine spatial resolutions. Time-advancement uses a so-called one-leg (one evaluation of fluxes per time step) scheme similar to the popular Adams–Bashforth scheme [32]. For

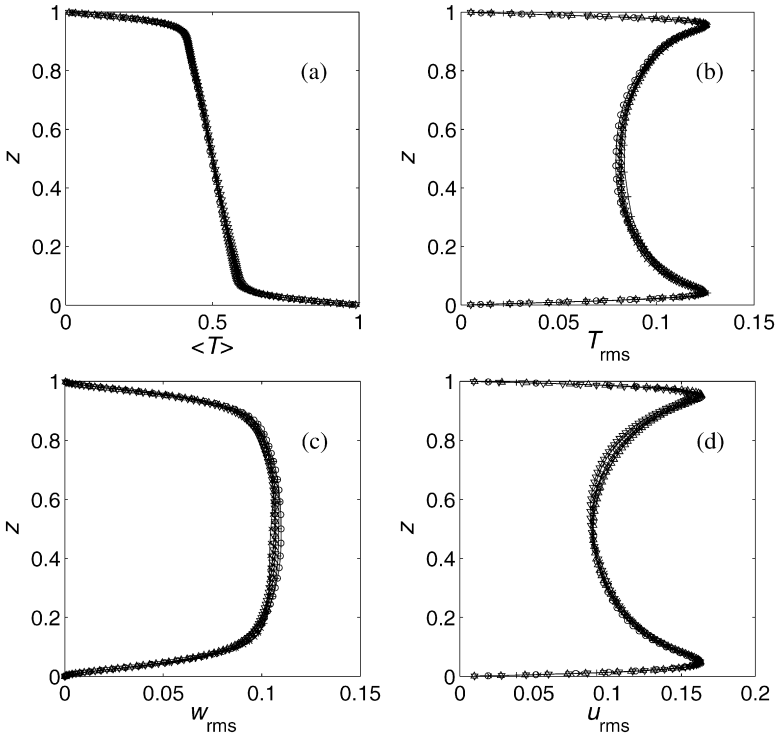

Fig. 1. Resolution and domain size check for the simulation at $Ra = 2.5 \times 10^6$, $Ro = 0.75$. (a) Average temperature. (b) Root-mean-square temperature. (c) Root-mean-square vertical velocity. (d) Root-mean-square horizontal velocity. The following cases are included: resolution $128 \times 128 \times 64$, domain size $2 \times 2 \times 1$ (circles, this case is taken from Table 1), resolution $128 \times 128 \times 128$, domain size $2 \times 2 \times 1$ (down triangles), resolution $64 \times 64 \times 32$, domain size $2 \times 2 \times 1$ (plusses), resolution $128 \times 128 \times 128$, domain size $1 \times 1 \times 1$ (up triangles), and resolution $64 \times 64 \times 64$, domain size $1 \times 1 \times 1$ (down triangles). Deviations from the reference case (resolution $128 \times 128 \times 64$, domain size $2 \times 2 \times 1$) are less than 3% for the mean temperature and less than 5% for the rms values.

further details on the numerical implementation and the validation for turbulent flow in a channel the reader is referred to Verstappen and Veldman [31].

Two series of simulations at different Ra have been performed. In these runs Ta was varied; the parameter settings and resolutions are summarised in Table 1. In all simulations the Prandtl number is set to $\sigma = 1$, a value comparable to that of air and cryogenic helium gas for which $\sigma \approx 0.7$. The latter is a popular convection fluid for experiments since very high Rayleigh numbers can be reached, see, e.g., Refs. [33,34]. The grid was uniform in the horizontal directions. A vertical distribution with a higher density of grid points near the walls is used to resolve the boundary layers. The simulation at $Ra = 2.5 \times 10^6$ and $Ro = 0.1$ is carried out as a special validation case, since convection should be suppressed by rotation with these parameters. Indeed, root-mean-square (rms) flow velocities do not exceed 10^{-6}, the linear temperature gradient remains and the Nusselt number remains 1 with seven digits of accuracy. The conductive state is thus well-reproduced.

Several *a posteriori* checks of resolution and domain size have been performed. One case ($Ra = 2.5 \times 10^6$, $Ro = 0.75$) has been considered at various resolutions and domain sizes. These are compared in Fig. 1. Specifically, the vertical profiles of (a) average temperature and (b) rms temperature, and (c) the rms of vertical velocity and (d) the rms of horizontal velocity are compared. A further discussion of the physical significance of these quantities is presented momentarily in Section 3.1. Here we restrict ourselves to assessing effects of domain-size and spatial resolution. Clearly, grid refinement and decrease of the domain size has very little influence on these statistics; even a coarsening of the grid still reproduces the results quite accurately.

Another issue is the resolution near the walls. The boundary layers that are formed near the bottom and top walls can be very thin compared to H. A suitable measure for their thickness is the minimum of the wall-normal distances (denoted by $d_{\min}$) at which the maximal rms of the temperature and velocity occur, for the thermal and viscous boundary layers, respectively. These thicknesses were reported in Kunnen et al. [22] at $Ra = 2.5 \times 10^6$. It was verified that in all simulations at least 9 grid points are located within $d_{\min}$. A similar procedure was carried out for the simulations at $Ra = 2.5 \times 10^7$. In all these simulations at least 10 grid points were found within $d_{\min}$. The near-wall resolutions are considered acceptable, as, for example, Verzicco and Camussi [35] find that six points clustered in the boundary layers give reliable results. A related validation of the near-wall resolution can be based on the Nusselt number calculated as the average wall-normal temperature gradient [22]. The Nusselt numbers in the validation runs (see caption of Fig. 1) were all within 1% of the reference case of Table 1. This close correspondence also establishes that the time-averaging process was performed over a sufficiently long flow-history (more details can be found in Kunnen et al. [22,36]).

As a final validation we compare the smallest turbulent length scales to the largest grid spacing in the domain. The smallest relevant length scale in this turbulent flow is estimated by the Kolmogorov length $\eta \equiv \nu^{3/4}/\epsilon^{1/4}$, where ϵ is the kinetic energy dissipation rate. In these convective flows the Batchelor scale $\eta_T \equiv \eta/\sigma^{1/2}$ is also relevant, but for unit Prandtl number it is equal to η and does not require separate consideration. An *a priori* estimate of the Kolmogorov length is $\eta = \sigma^{1/2}/[Ra(Nu-1)]^{1/4}$ [37]. In all simulations we verified that the maximal grid spacing was always smaller than 4η, a criterion found to be sufficient in Refs. [29,35]. Our grid-requirement is actually stricter than these references. The maximal vertical grid-point spacing is found at $z = 0.5$. There the local dissipation rate is smallest and the local Kolmogorov scale is thus considerably larger than the *a priori* estimate would suggest.

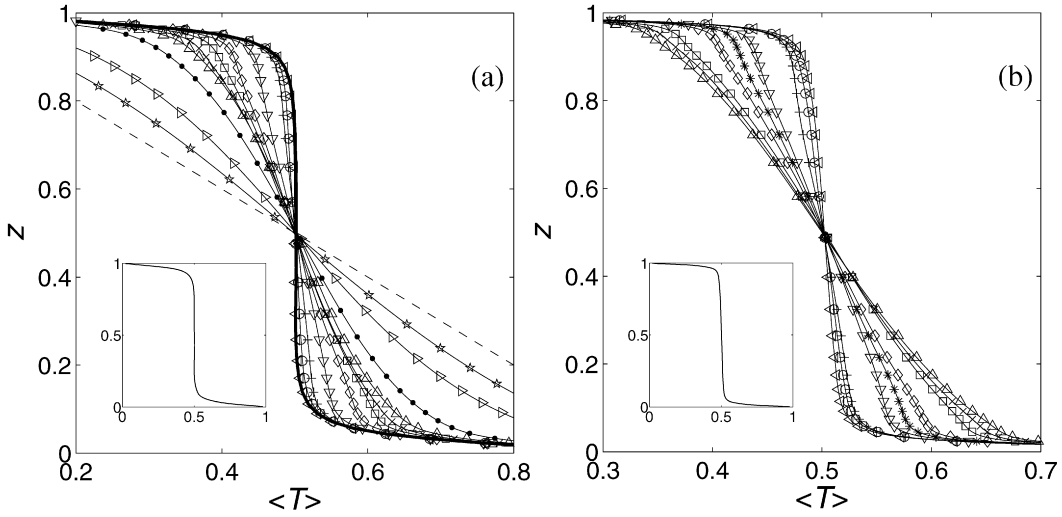

Fig. 2. Average temperature profiles, $\langle T\rangle$, as a function of z, for: (a) $Ra = 2.5 \times 10^6$, (b) $Ra = 2.5 \times 10^7$. The curves are: $Ro = \infty$ (thick solid line), $Ro = 4.00$ ($\triangleleft$), $Ro = 3.20$ ($\circ$), $Ro = 2.50$ ($+$), $Ro = 1.33$ ($\triangledown$), $Ro = 1.00$ ($*$), $Ro = 0.75$ ($\diamond$), $Ro = 0.50$ ($\square$), $Ro = 0.40$ ($\times$), $Ro = 0.33$ ($\triangle$), $Ro = 0.25$ ($\bullet$), $Ro = 0.16$ ($\triangleright$), $Ro = 0.13$ ($\star$), and $Ro = 0.10$ (dashed line). Note that the horizontal axis does not represent the full temperature range. The insets of (a) and (b) are the $Ro = \infty$ and $Ro = 4.00$ curves plotted for the full temperature range $(0-1)$, respectively. At $Ra = 2.5 \times 10^7$ no $Ro = \infty$ case is simulated.

3. Rotational dependence of flow statistics

In this section the averaged vertical profiles of velocity, vorticity and temperature are discussed first (Section 3.1). Then the probability density functions of temperature, velocity and vorticity are presented (Section 3.2). In Section 3.3 the turbulent kinetic energy balance is examined.

3.1. Vertical profiles for temperature, velocity and vorticity

We start the presentation of the results with quantities averaged over time and over the horizontal directions. These provide a general overview of the influence of rotation on convection. In Fig. 2 the vertical profile of the average temperature $\langle T\rangle$ is presented, at both Rayleigh numbers and all Rossby numbers included in this study. For the non-rotating case (thick solid line in the left panel) the well-known profile consisting of two boundary layers connecting the well-mixed bulk to the walls is recovered (see also, e.g., Kerr [38]). As rotation is introduced, a negative temperature gradient in the bulk persists. Its magnitude is dependent on Ro. The gradient in the bulk should become equal to -1 when Ro is lower than the critical Rossby number. This applies at $Ro_c \simeq 0.127$ for $Ra = 2.5 \times 10^6$ and at $Ro_c \simeq 0.072$ when $Ra = 2.5 \times 10^7$. At $Ra = 2.5 \times 10^6$ and $Ro = 0.10$ indeed the linear gradient is conserved (dashed line in the left panel).

We have calculated the gradient of average temperature $\langle T\rangle$ at the half-height ($z = 0.5$) and plotted it against Ro in Fig. 3. Here it can be seen that for most of the Ro range the gradient is roughly independent of Ra, as the filled and open symbols coincide rather well. This observation was also made by Julien et al. [10], who investigated the gradient as a function of Ra for constant $Ro = 0.75$. As Ro approaches Ro_c a sudden increase of the magnitude of the gradient is found, rapidly approaching the conductive value of -1. This can be interpreted as a 'laminarisation' of the flow under the constraint imposed by strong rotation. It must be emphasised that at the higher $Ra = 2.5 \times 10^7$ the strongly decreased gradient is expected close to $Ro_c = 0.072$, passing well beyond the current parameter range. Therefore, the rapid deviation is only found at the lower $Ra = 2.5 \times 10^6$ with the Ro values chosen here.

The non-zero bulk temperature gradient under rotation has been treated in some previous studies [10,39] and its dependence on the Prandtl number has also been discussed [9]. Julien et al. [10]

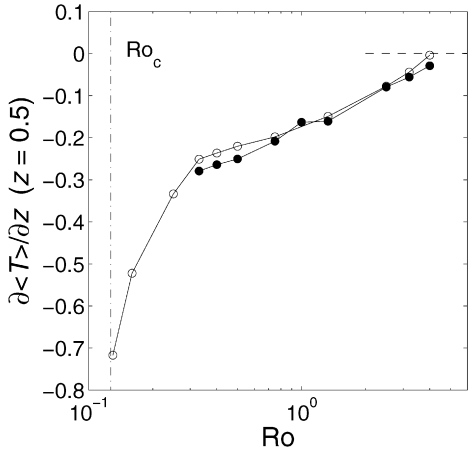

Fig. 3. Mid-plane temperature gradient as a function of Ro. Open symbols are for $Ra = 2.5 \times 10^6$, while filled symbols correspond to $Ra = 2.5 \times 10^7$. The dashed line on the right-hand side indicates the zero gradient at $Ro = \infty$. Also included is the critical Rossby number $Ro_c = 0.127$ of linear stability for $Ra = 2.5 \times 10^6$ (dash-dotted line).

present a possible explanation for the non-zero bulk temperature gradient under rotation. The background rotation causes increased vorticity, aligned with the rotation, in the flow. Like-signed vortical structures show mutual interactions, as occurs in two-dimensional flows (especially vortex merger, see, e.g., [40,41]). Through the vortex merging horizontal mixing is enhanced relative to vertical mixing. As a result, the lower half of the domain remains warmer and the top half cooler; increased thermal conduction balances the unstable gradient. In [10] it is also put forward that this effect should be dependent on Ro, but not on Ra when Ro is taken constant. This is indeed observed in our simulations: variation of Ra at constant Ro indeed does not drastically change the magnitude of the gradient, at least not for the current parameter range.

In order to investigate fluctuations in the temperature fields, we turn to the rms of the temperature. This property is defined here as $T_{\rm rms} = \sqrt{\langle (T - \langle T\rangle)^2\rangle}$ in terms of averages over horizontal planes and over time. The vertical profiles of $T_{\rm rms}$ are depicted in Fig. 4. The profile obtained in the non-rotating case is very similar to that found by Kerr [38]. The highest rms values occur near the walls. When rotation is added the boundary-layer behaviour

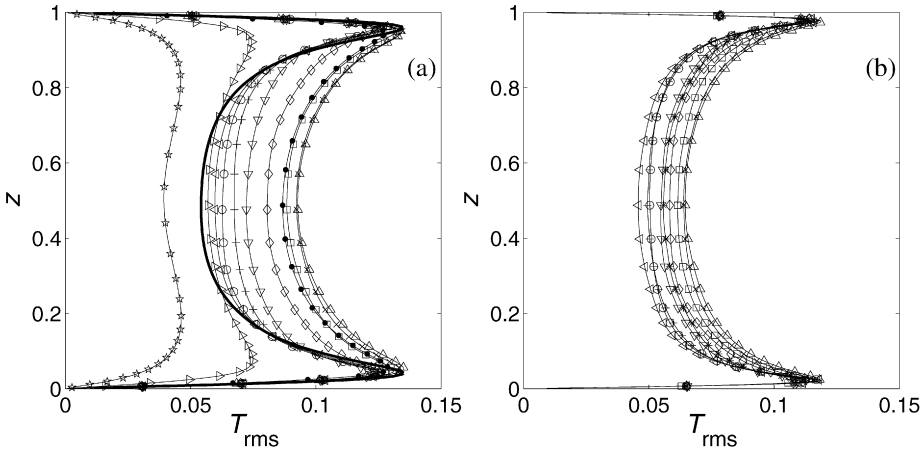

Fig. 4. Root-mean-square temperature fluctuations, T_{rms}, as a function of z, for: (a) $Ra = 2.5 \times 10^6$, (b) $Ra = 2.5 \times 10^7$. The curves are labelled as in Fig. 2.

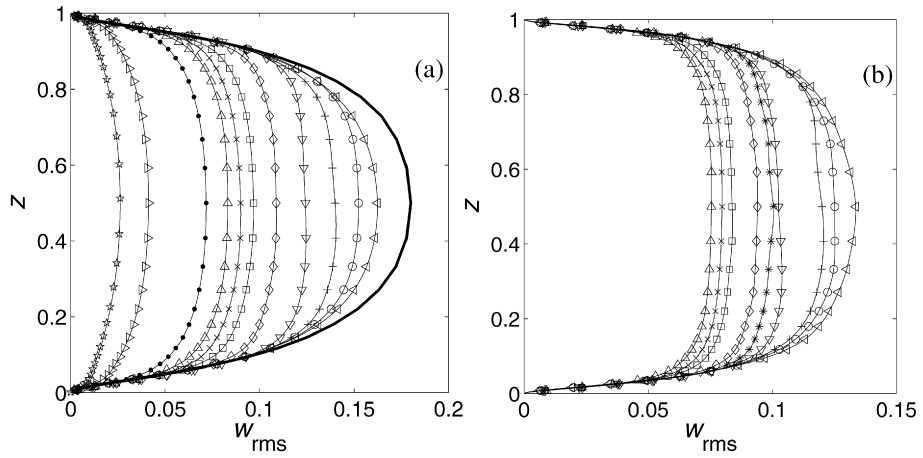

Fig. 5. Vertical rms velocities, w_{rms}, as a function of z, for: (a) $Ra = 2.5 \times 10^6$, (b) $Ra = 2.5 \times 10^7$. The curves are labelled as in Fig. 2.

is not affected much. In the bulk, however, a strong increase of the fluctuations is noticed, which can be explained as follows. The plumes originate and are fed at vertical positions closer to the bottom (top) plates (see the discussion of the skewness of vertical velocity in Kunnen et al. [22]), and thereby are fed with warmer (cooler) fluid than without rotation. However, this behaviour does not persist to the asymptotic range of very low Ro. In fact, in the lowest-Ro cases in Fig. 4(a) a rapid decrease of the fluctuations is noticed, confirming the laminarisation under sufficiently strong rotation. At the higher Ra the effects of rotation are less profound as all cases considered are still highly supercritical, i.e., $Ro \gg Ro_c$.

We next proceed with the velocity, and first consider the rms of the vertical velocity $w_{rms} = \sqrt{\langle w^2 \rangle}$ in Fig. 5. Notice that it is meaningless to consider $\langle w \rangle$; since we are taking a planar average, the average vertical velocity must by definition be zero due to incompressibility. The profiles of w_{rms} reach their maximal value in the central region. The stabilising effect of rotation is directly observable: with decreasing Ro the profiles are lowered, approaching zero in the steady limit at Ro_c. When comparing the two Ra values studied, it is found that at the higher Ra value the spreading in rms velocities as function of Ro is smaller. Indeed, at higher Ra the flow is more turbulent at the adopted values for Ro, being farther from the steady conductance value Ro_c than in the lower Ra case.

For the treatment of the horizontal velocity components we follow the definition of Kerr [38]:

$$u_{rms} = \sqrt{\langle u^2 \rangle + \langle v^2 \rangle}, \tag{7}$$

where it is implied that $\langle u \rangle \approx \langle v \rangle \approx 0$. The correctness of this assumption was verified separately. In Fig. 6 the vertical profiles of u_{rms} are shown. From these results we clearly infer that also horizontal fluctuations decrease with increasing rotation rates. Interestingly, we observe in Fig. 6(a) that in the central region the curve corresponding to $Ro = 4$ (with left triangles) is at a higher value than in the non-rotating $Ro = \infty$ case (thick solid line). This arises since the plumes are spun up while accelerating away from the walls, thereby gaining horizontal velocity. This is only a rather small effect and rapidly the overall damping effect of rotation becomes dominant: the flow is driven in the vertical direction by buoyancy, and thus if vertical velocities decrease the horizontal components must follow suit.

As a summary of the previous results we plot the mid-plane rms values of temperature, and, horizontal and vertical velocity as a function of Ro in Fig. 7. The velocity statistics all show a similar trend as a function of Ro. The values have an approximate power-law dependence on Ro for a wide range of rotation rates. For sufficiently low values of Ro approaching Ro_c a sudden drop of velocity fluctuations towards zero occurs. Temperature fluctuations have an opposite correlation for large Ro, and show the same asymptotic decrease toward zero near Ro_c. The fitted power laws for the scaling ranges are printed in Table 2. A comparison of the two Rayleigh number cases shows that the relative fluctuations of both velocity and temperature are smaller at higher Ra in the scaling adopted here. Their dimensional forms do increase when Ra is increased. A comparison of numerical values for $Ra = 2.5 \times 10^6$, $Ro = 0.75$ with the results reported in literature by Julien et al. [10]

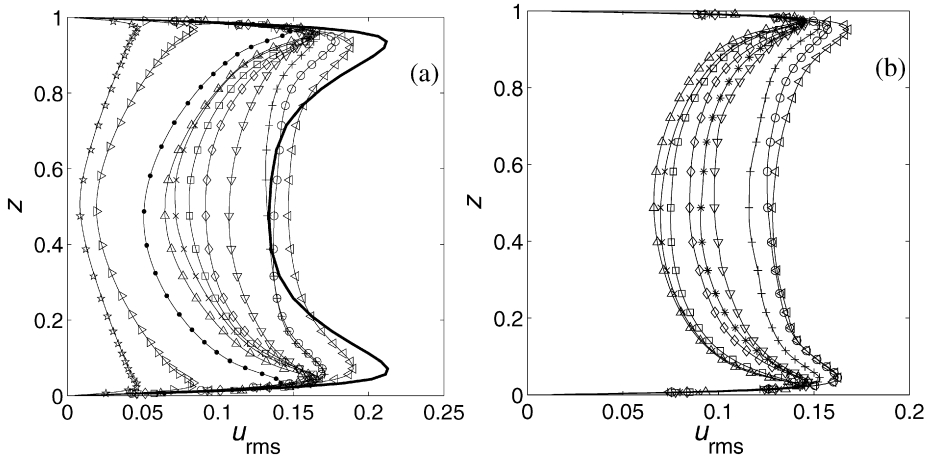

Fig. 6. Horizontal rms velocities, u_{rms}, as a function of z, for: (a) $Ra = 2.5 \times 10^6$, (b) $Ra = 2.5 \times 10^7$. The curves are labelled as in Fig. 2.

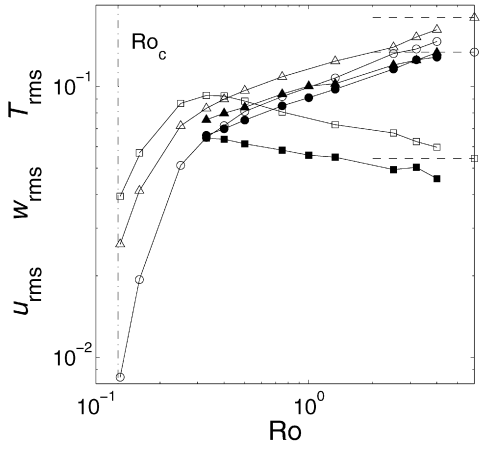

Fig. 7. Mid-plane rms values as a function of *Ro*. Open symbols are for $Ra = 2.5 \times 10^6$, while filled symbols correspond to $Ra = 2.5 \times 10^7$. Included are u_{rms} (circles), w_{rms} (triangles), and T_{rms} (squares). The dashed lines with open symbols on the right-hand side indicate the corresponding values for $Ro = \infty$ at $Ra = 2.5 \times 10^6$. Also included is the critical Rossby number $Ro_c = 0.127$ of linear stability for $Ra = 2.5 \times 10^6$ (dash-dotted line).

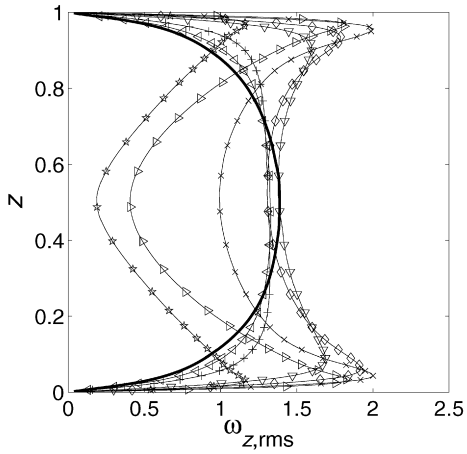

Fig. 8. Root-mean-square vorticity, $\omega_{z,rms}$, as a function of z, for $Ra = 2.5 \times 10^6$ and: $Ro = \infty$ (thick solid line), $Ro = 4.00$ ($\triangleleft$), $Ro = 2.50$ ($+$), $Ro = 1.33$ ($\triangledown$), $Ro = 0.75$ ($\diamond$), $Ro = 0.4$ ($\times$), $Ro = 0.16$ ($\triangleright$) and $Ro = 0.13$ ($\star$).

Table 2
Power laws fit to the root-mean-square velocities and temperatures of Fig. 7. The fits are applied for $0.33 \leqslant Ro \leqslant 4$.

	$Ra = 2.5 \times 10^6$	$Ra = 2.5 \times 10^7$
u_{rms}	$(0.097 \pm 0.002)\, Ro^{0.31 \pm 0.01}$	$(0.0903 \pm 0.0004)\, Ro^{0.272 \pm 0.005}$
w_{rms}	$(0.114 \pm 0.001)\, Ro^{0.254 \pm 0.009}$	$(0.0980 \pm 0.0005)\, Ro^{0.221 \pm 0.006}$
T_{rms}	$(0.0773 \pm 0.0006)\, Ro^{-0.178 \pm 0.007}$	$(0.0563 \pm 0.0003)\, Ro^{-0.129 \pm 0.008}$

shows excellent agreement: here we find $T_{rms} = 0.0795$, compared to $T_{rms} = 0.0793$ of Julien et al. (with the value adapted to our scaling). Considering the vertical velocity, $w_{rms} = 0.108$ from this work is to be compared to $w_{rms} = 0.110$ (same adaptation of the scaling of Julien et al.).

One of the prominent dynamic effects of the presence of background rotation is the introduction of strong vertical vorticity $\omega_z = (\nabla \times \mathbf{u})_z$ into the flow field near the no-slip walls. As fluid converges towards a site at which a plume forms inside the boundary layer, it is spun up cyclonically, gaining positive ω_z. While the plume crosses the bulk its excess vorticity is gradually lost and even anticyclonic vorticity may appear during spin-down and radial outflow on the other side of the domain. The flow phenomenology is described well as a collection of vortical plumes through which vertical transport of heat and momentum takes place [9,10,18,28,42–45].

To quantify the effects of *Ro* on the vertical vorticity we focus on some characteristic *Ro* values at $Ra = 2.5 \times 10^6$. We include $Ro = \infty$ as a (non-rotating) reference case, $Ro = 4.00$, 2.50, 1.33, 0.75, 0.40, 0.16 and 0.13. In Fig. 8 we show the vertical profiles of the rms vertical vorticity $\omega_{z,rms}$. It is verified that in all simulations the horizontal planar average $\langle \omega_z \rangle$ is zero at all vertical positions. The profile for $Ro = \infty$ is reminiscent of the w_{rms} profile in Fig. 5, with a broad maximum around the mid-plane. In case rotation is added, for $Ro < 2.50$, two maxima arise close to the sidewalls, corresponding to the spin-up of converging fluid feeding the plumes. The vertical position of the maxima matches well with the position of the maxima in u_{rms} (cf. Fig. 6), reinforcing the notion that the spin-up is a boundary-layer effect. The bulk value does not change much under rotation for a wide range of *Ro* values. Only at strong rotation (here for cases $Ro = 0.4$ and lower) a decrease in central $\omega_{z,rms}$ is experienced. Furthermore, we observe that the highest $\omega_{z,rms}$ value is not simply found in the case of highest rotation (lowest *Ro*), but here around $Ro = 0.4$. Apparently, at a sufficiently low value of *Ro* the stabilising effect of rotation becomes so important that it effectively suppresses fluid motion.

To further characterise the effect of rotation on vorticity, we concentrate on the vertical-vorticity skewness $S_{\omega_z} = \langle \omega_z^3 \rangle / \omega_{z,rms}^3$. This is a measure for the asymmetry of the cyclonic/anticyclonic vorticity distribution. In Fig. 9, we plotted vertical profiles of S_{ω_z}. A positive value of S_{ω_z} indicates that strong cyclonic (positive) vorticity is preferred by the system, with weaker anticyclonic (neg-

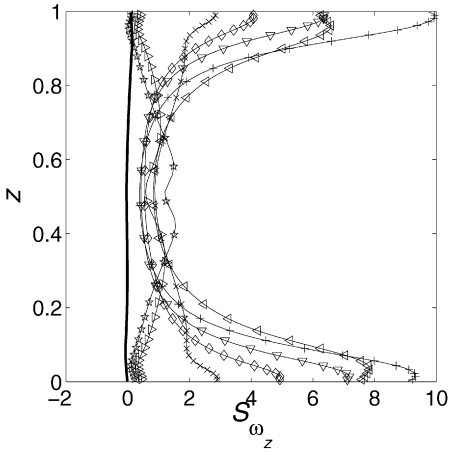

Fig. 9. Skewness of vorticity, S_{ω_z}, as a function of z, for $Ra = 2.5 \times 10^6$. Symbols as in Fig. 8.

ative) vorticity filling a larger portion of the domain to retain the required zero average vorticity over horizontal cross-sections. Intuitively, one would expect the skewness to be larger at higher rotation rate, but it is found that the dependence is not monotonous. In fact, there is a rotation-rate at which skewness is most pronounced, see Fig. 9. Without rotation the vorticity distribution is virtually symmetric at all heights. Correspondingly $S_{\omega_z} \approx 0$, as indicated by the thick solid line. For the cases with non-zero rotation in Fig. 9 there is positive skewness throughout the layer. At the mid-plane S_{ω_z} is only very weakly dependent on Ro, while close to the walls large differences are found. There is a strongly anti-symmetric vorticity distribution near the walls for intermediate Ro, maximal near $Ro = 2.5$, while the skewness for very low Ro (e.g., in case $Ro = 0.16$) tends toward zero near the walls and becomes largest in the central region. This points at a change in flow structuring. At $Ro \gtrsim 0.4$ a turbulent state is found, with localised 'bursts' of vorticity formed near the walls and then penetrating the bulk of the domain (cf. the visualisations in [10]). At lower Rossby numbers these bursts of vorticity can cover the entire vertical extent of the domain and a clear columnar structuring is observed. We discussed this particular columnar structuring in more detail in [46], where a visualisation of the columns and ensemble-averaged profiles of velocity, temperature, and vorticity are presented for the vortical columns. The columns are near-symmetrical in the vertical direction. The mid-plane vorticity asymmetry is somewhat larger than in the turbulent state. The skewness of vorticity has also been discussed by Vorobieff and Ecke [45], but differences in domain composition (a cylinder with rigid walls was used by Vorobieff and Ecke compared with our horizontally periodic box) and Prandtl number (Vorobieff and Ecke used $\sigma = 5.81$ while here $\sigma = 1$) prevent a more detailed comparison here. Julien et al. [10] also discuss S_{ω_z}. For $Ra = 2.5 \times 10^6$, $Ro = 0.75$ only the extremal value $S_{\omega_z} \approx 4.5$ is given, which matches very well with the extremal value observed in the current simulations.

The tendency for extreme values of vorticity to occur in the flow can be quantified with the kurtosis $K_{\omega_z} = \langle \omega_z^4 \rangle / \omega_{z,\mathrm{rms}}^4$. A high kurtosis indicates that extreme values occur frequently. For reference, the kurtosis of a Gaussian distribution is 3, while an exponential distribution has a kurtosis of 6. In Fig. 10 the kurtosis is depicted as a function of the vertical coordinate z. In absence of rotation the kurtosis is nearly constant at a value close to 6 in the central region, with a slight increase near the walls. The addition of a relatively weak rotation ($Ro = 2.5$ or $Ro = 4.0$) has a dramatic effect on the kurtosis near the walls. The considerably higher kurtosis points to the occurrence of vorticity near the walls of magnitude many times $\omega_{z,\mathrm{rms}}$. Also at $Ro = 0.75$ and $Ro = 1.33$ there are pronounced maxima near the walls, but since $\omega_{z,\mathrm{rms}}$ is considerably larger near the walls for these Rossby numbers the numerical value of K_{ω_z} is not as large. At the two lowest Ro considered here, the near-wall kurtosis approaches the value 3. Also for a Gaussian distribution $K = 3$. In the central bulk region, however, K_{ω_z} becomes the largest of all cases considered here. This is an additional effect of the columnar structuring.

3.2. Probability density functions of velocity, temperature and vorticity

Changes in flow properties due to rotation, at large and small scales can be illustrated by computing the probability density function (PDF) of several characteristic properties. We include PDFs of vertical velocity, temperature and vertical vorticity at two vertical positions: at mid-height ($z = 0.5$) and at $z \approx 0.05$ close to the bottom wall. Results for two Rayleigh numbers at the same Rossby number of $Ro = 1.33$ are compared in Fig. 11, while the influence of rotation is assessed at constant $Ra = 2.5 \times 10^6$ for several rotation rates, i.e., at $Ro = \infty, 0.75, 0.16$ in Fig. 12.

Starting with the constant-Ro, variable Ra comparison of Fig. 11, it is found that the bulk PDFs are similar in shape for both Ra values considered. Vertical-velocity and temperature distributions are nearly Gaussian. In the temperature PDFs the transition to a near-exponential shape, found earlier in non-rotating convection in cylindrical domains for high $Ra \gtrsim 4 \times 10^7$ and $\sigma = 0.7$ [33,47], is indeed not observed at the current Ra values. The exponential distribution was postulated to be caused by intermittent releases of thermal plumes from the boundary layers. Exponential temperature PDFs have subsequently also been found in water ($\sigma \approx 5$) [48] and in mercury ($\sigma \approx 0.02$) [49]. In the rotating case there is both numerical [10] and experimental [50] evidence that the temperature PDF remains close to Gaussian, which is confirmed here. Exponential vorticity PDFs are recovered, as in Refs. [10,30], emphasising the structuredness of the vorticity field into localised regions of strong vorticity [30]. The slight positive skewness was already noted in Fig. 9.

Closer to the wall the distributions change considerably. At $Ra = 2.5 \times 10^6$ the vertical-velocity PDF, shown by the solid line in Fig. 11(d), is strongly skewed towards positive values, i.e., strong motion directed away from the wall is favoured [22]. The effect is almost absent for the higher Ra distribution. This is due to the fact that the vertical position at which the PDF was recorded is just outside the (thinner) boundary layer: at $Ra = 2.5 \times 10^6$ ($Ro = 1.33$) the viscous boundary layer thickness is $\delta_\nu = 0.053$, while at $Ra = 2.5 \times 10^7$ ($Ro = 1.33$) it is $\delta_\nu = 0.034$ (δ_ν is based on position of maximal rms velocity). A Gaussian distribution is recovered there. The occurrence of a skewed distribution is thus strongly coupled with the boundary layer region, as it is within the boundary layer that the vortical plumes originate.

The temperature PDFs are 'cut off' on the right-hand side by the temperature boundary condition on the wall. The sum of mean temperature plus any fluctuations must always remain between 0 and 1. This condition, with the rather high mean temperature at this height (see Fig. 2, at $z \approx 0.05$), does not allow strong positive temperature fluctuations, therefore the sudden drop on the right-hand side of these PDFs. Mainly for the higher Ra-value the distribution is skewed towards higher temperature, which is indicative of the 'warm' vortical tubes that originate near the bottom wall.

Vorticity PDFs are extremely skewed to the right (see also Fig. 9), pointing to the formation of the vortical tubes possessing strong cyclonic (positive) vorticity that were discussed earlier. The very broad tail on the right-hand side is responsible for the large kurtosis observed near the walls in Fig. 10.

We proceed with the comparison of PDFs at various Ro, while keeping $Ra = 2.5 \times 10^6$, given in Fig. 12. The non-rotating ($Ro = \infty$,

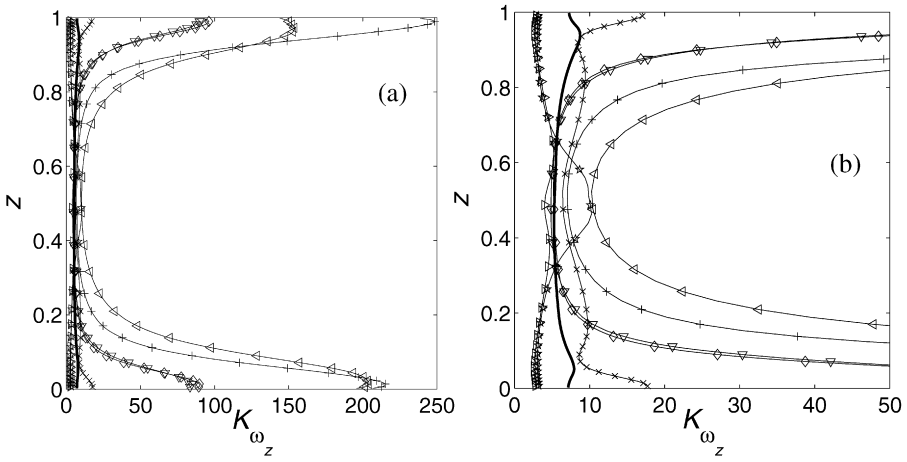

Fig. 10. Kurtosis of vorticity, K_{ω_z}, as a function of z, for $Ra = 2.5 \times 10^6$. Symbols as in Fig. 8. (a) Full range. (b) Close-up of the lower K_{ω_z} values.

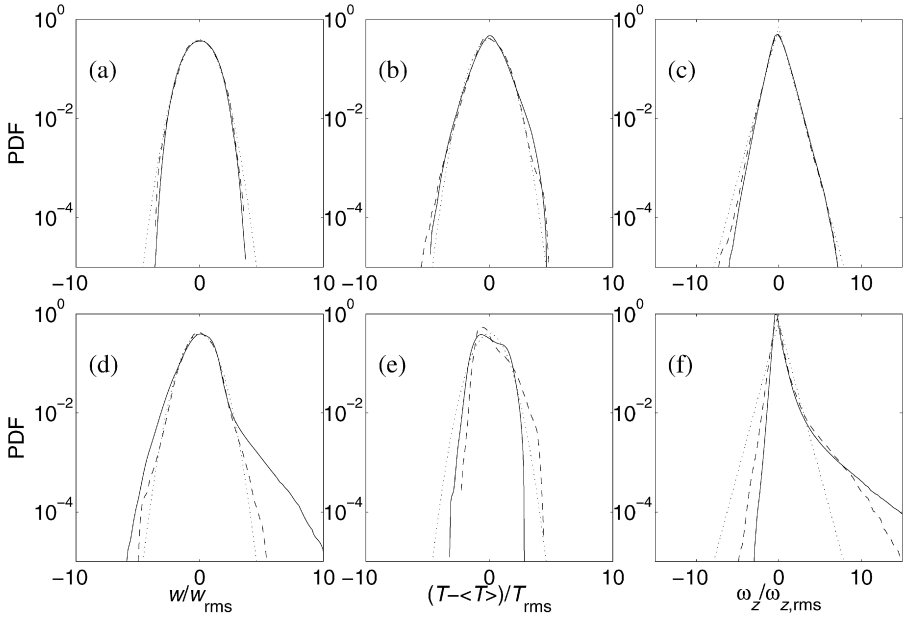

Fig. 11. PDFs of various flow properties at $Ro = 1.33$ for $Ra = 2.5 \times 10^6$ (solid lines) and $Ra = 2.5 \times 10^7$ (dashed lines). The top row (a)–(c) is for the mid-plane $z = 0.5$, while the bottom row (d)–(f) is taken close to the lower wall at $z \approx 0.05$. Quantities included are: (a), (d) vertical velocity w, (b), (e) temperature T, and (c), (f) vertical vorticity ω_z. The dotted lines in (a), (b), (d), (e) are reference Gaussian distributions; dotted lines in (c), (f) are reference exponential distributions.

solid lines) distributions reported here show a good agreement with those of Balachandar and Sirovich [51]. Vertical velocity has a narrower-than-Gaussian shape in the centre, while near the wall a considerable negative skewness is found [22]. The temperature PDF at the mid-plane has exponential tails related to strong fluctuations [51] but the tails must be bounded at finite temperatures by the boundary conditions. Near the wall a similar distribution to that of Fig. 11(e) is found. Exponential distributions are found for vorticity, just as Balachandar and Sirovich report [51].

The addition of a moderate rotation (displayed at $Ro = 0.75$ by the dash-dotted lines, and by the solid lines at $Ro = 1.33$ in Fig. 11) provides Gaussian velocity and temperature statistics at the mid-plane [10]. The vorticity PDF remains exponential, with a slight positive skewness. Julien et al. [30] draw parallels with the so-called 'hard turbulent convection' [33,47] based on these exponential PDFs and their reported $Nu \sim Ra^{2/7}$ scaling that is also recovered at $Ro = 0.75$, as these two findings are characteristic for the hard turbulent convection. Near the wall the skewness of the velocity PDF changes sign. We elaborated on this observation in Ref. [22]. For the vorticity the strong positive skewness is appreciated.

At the highest rotation rate ($Ro = 0.16$, dashed lines) a trend toward Gaussian statistics is found in all PDFs. Thus a state is achieved in which the vortical plumes are not as dominant, in the sense that extreme vorticity fluctuations are much rarer. The vorticity distributions retain a small positive skewness. This indicates that a near-equilibrium between the number of cyclonic and anticyclonic vortical tubes is reached in contrast with the strongly skewed ratio for moderate rotation [45].

3.3. Kinetic energy budget

The dynamics of turbulent flow in the Rayleigh–Bénard configuration, and the influence of rotation on it can be characterised further by concentrating on the kinetic energy. The budget equation for the averaged turbulent kinetic energy $\langle E \rangle = \langle (u^2 + v^2 + w^2)/2 \rangle$ in convection is [52–54]

$$\langle wT \rangle + \sqrt{\frac{\sigma}{Ra}} \frac{\partial^2}{\partial z^2} \langle E \rangle - \frac{\partial}{\partial z} \langle wE \rangle - \frac{\partial}{\partial z} \langle wp \rangle - \epsilon = 0, \tag{8}$$

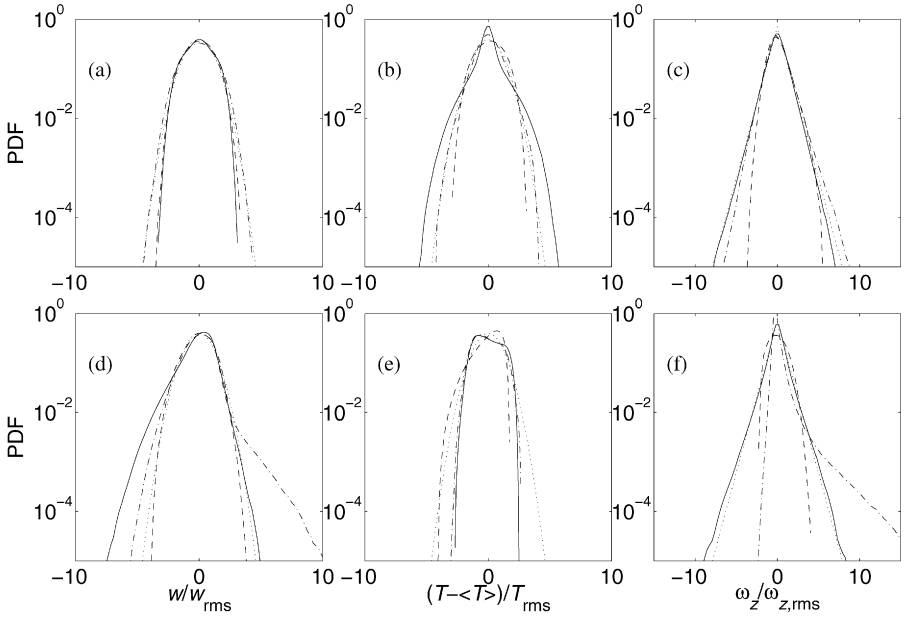

Fig. 12. PDFs of various flow properties at $Ra = 2.5 \times 10^6$ for $Ro = \infty$ (solid lines), $Ro = 0.75$ (dash-dotted lines) and $Ro = 0.16$ (dashed lines). The top row (a)–(c) is for the mid-plane $z = 0.5$, while the bottom row (d)–(f) is taken close to the lower wall at $z \approx 0.05$. Quantities included are: (a), (d) vertical velocity w, (b), (e) temperature T, and (c), (f) vertical vorticity ω_z. The dotted lines are reference Gaussian or exponential distributions.

where $\langle\cdot\rangle$ denotes averaging over a sufficiently long time and over the horizontal directions. The first term is the buoyant production, the second term is due to molecular dissipative transfer, the third is the turbulent transport term, the fourth is the pressure transport term, and the fifth is the dissipation rate $\epsilon = \sqrt{\sigma/Ra}(\nabla\mathbf{u} : (\nabla\mathbf{u})^T)$. A remark must be made concerning the third term (turbulent transport): in case of the presence of a mean horizontal velocity V the term $-\partial\langle wE\rangle/\partial z$ also contains production of kinetic energy by shear $-\langle vw\rangle(\partial V/\partial z)$ [54]. Although not completely equivalent to the large-scale circulation of confined convection, a global organisation of the mean flow is also found in horizontally periodic domains [55–57]. These large-scale flows may produce turbulent kinetic energy through shear production.

In the statistically stationary state, averaging over sufficiently long time implies that $d\langle E\rangle/dt = 0$. The addition of rotation does not change this equation directly. However, the balance of these terms may change indirectly, thus characterising rotational effects.

In Fig. 13 we present the five terms in the budget equation (8) and their dependence on z at $Ra = 2.5 \times 10^6$ for four different Rossby numbers, viz. $Ro = \infty, 1.33, 0.75$ and 0.16. The case $Ro = \infty$ in Fig. 13(a) shows profiles very similar to those reported in Refs. [52–54]. The conjecture of Kerr [54] that pressure transport (dash-dotted line) dominates over turbulent transport (thin solid line) in the boundary layer ($z \gtrsim 0.9$) is readily confirmed by our simulations. A consequence is that shear production is not important in the boundary layer; instead, pressure transports energy from the bulk into the boundary layer [54,57], where it is dissipated. This contrasts with the energy budget for the boundary layer in turbulent channel flow [58] where the kinetic energy is actively produced by the shear in the boundary layer, and pressure transport is found to be only a small contribution. Very close to the wall the energy budget basically consists of a balance between molecular transfer (dotted line) and dissipation (dashed line). In the bulk the buoyant production is seen to be balanced predominantly by the dissipation term, with some contribution from the pressure-driven transport of energy to the boundary layers.

Under strong rotation [e.g., Fig. 13(d)], all terms in the budget are strongly reduced. This shows that under these conditions the turbulence intensity is considerably lowered, as already discussed previously. At moderate rotation-rates, cf. Figs. 13(b), (c), only quite gradual changes in the budget can be observed for most of the terms, compared to the non-rotating case. No qualitative changes are observed except in the turbulent transport, which is seen to change sign under rotation. At zero rotation there is turbulent transport of energy from the boundary layer into the bulk, while under rotation this transport is reversed. These changes are better interpreted with a plot showing actual changes in the various terms by subtracting the corresponding $Ro = \infty$ terms.

Changes in the production and dissipation terms relative to the non-rotating case are of interest to understand effects of rotation. These are collected in Fig. 14, where the differences between contributions from the rotating- and the non-rotating case are displayed. The buoyant production terms show an increased value close to the boundaries, while the difference in the bulk is very small. This is an indication of the added vertical heat transfer under moderate rotation. Under these conditions, rotation expresses itself by increasing the amount of fluid with a higher thermal contrast, from regions close to the walls, to participate in the buoyant production.

The dissipation is seen to be redistributed in Fig. 14: in the (thinner) boundary layers the dissipation is reduced, while an increase is found throughout the bulk. Due to the formation of vortical plumes with considerable horizontal velocity, stronger horizontal velocity *gradients* are formed between the plumes outside of the boundary layers. Thereby the dissipation is increased. The boundary layers have a reduced thickness, and the dissipation inside the layers is smaller.

Now we can address the changes in the turbulent transport term under rotation. The vertical profile of this term *without* subtraction of the corresponding $Ro = \infty$ profile, but divided by 20, is also included in Fig. 14. It can be concluded that the turbulent transport term represents the Ekman transport of the buoyant production maxima of Fig. 14 toward the bulk, where the extra dissipation is now found. Quantitatively these graphs do not show the full redistributions: actually all the transport terms change in magnitude (not shown explicitly), but only the turbulent transport term shows a radically different behaviour due to the presence of background rotation.

In Fig. 15 we presented the kinetic energy budget at the larger $Ra = 2.5 \times 10^7$, with $Ro = 1.33$. It is found that the dimension-

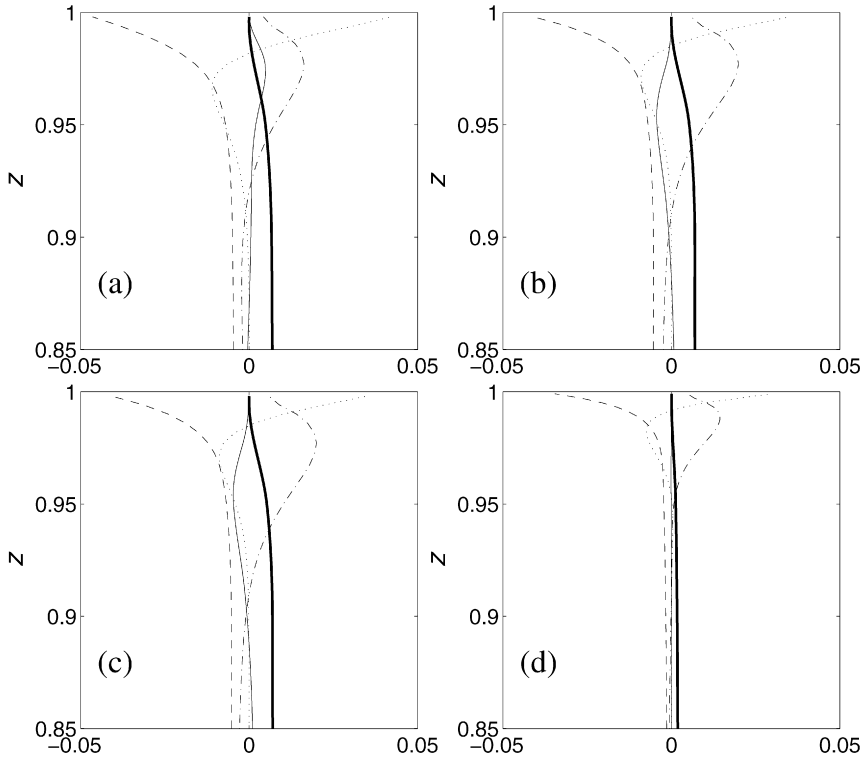

Fig. 13. Kinetic energy budget. Terms shown are: $\langle wT\rangle$ (thick solid line), $\sqrt{\sigma/Ra}\partial^2\langle E\rangle/\partial z^2$ (dotted line), $-\partial\langle wE\rangle/\partial z$ (thin solid line), $-\partial\langle wp\rangle/\partial z$ (dash-dotted line), $-\epsilon$ (dashed line). Included are: (a) $Ro=\infty$, (b) $Ro=1.33$, (c) $Ro=0.75$, (d) $Ro=0.16$. The curves are symmetrical in $z=0.5$. Only $0.85\leqslant z\leqslant 1$ is shown; the terms remain approximately constant for $0.15\leqslant z\leqslant 0.85$.

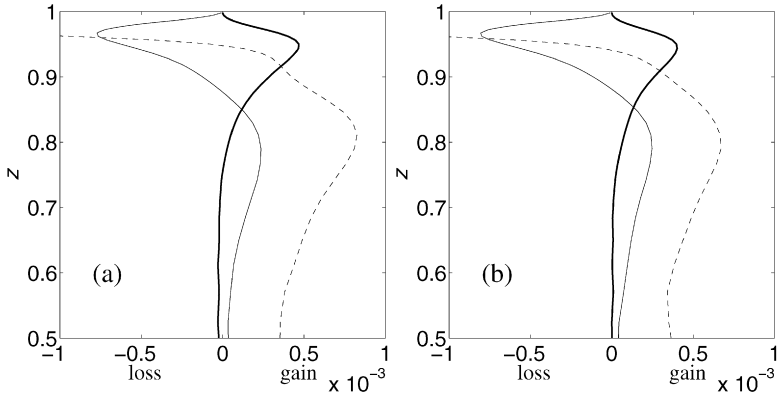

Fig. 14. Differences from $Ro=\infty$ [Fig. 13(a)] of buoyant production $\langle wT\rangle_{Ro}-\langle wT\rangle_{Ro=\infty}$ (thick solid line) and dissipation $\epsilon_{Ro}-\epsilon_{Ro=\infty}$ (dashed line) terms for (a) $Ro=1.33$ and (b) $Ro=0.75$. The thin solid line is the full term $-\partial\langle wE\rangle/\partial z$, divided by 20 for scale.

less numerical values decrease (notice the change of scale on the horizontal axis compared to Fig. 13). This is just an effect of the nondimensionalisation with the *Ra*-dependent velocity and time scales that are used in this paper. The other features of the energy budget are very similar to those seen at the lower value of *Ra*, with the exception that the boundary-layer region is thinner at the higher *Ra*-value.

4. Conclusions

Effects of rotation on turbulent Rayleigh–Bénard convection have been assessed with direct numerical simulation. The results show that rotation stabilises the flow, i.e., averaged turbulence intensities decrease. Curiously, there is a range of rotation rates, where, in spite of the reduced turbulent intensity, the heat transfer is increased relative to the non-rotating situation [15,18,19,22,23,26]. The Ekman boundary layer that connects the vortical plumes to the walls 'pumps' fluid from very close to the wall (and thus with considerable thermal contrast) into these plumes [9,10]. Hence an added vertical fluid transport takes place which also increases the heat transfer. This added Ekman transport is also observed in the kinetic energy budget of the flow.

Another important effect is the average temperature gradient over the fluid bulk [10,39]. The gradient is shown to be dependent on *Ro*, but not so much on *Ra* at constant *Ro* [10]. Increased lateral mixing, indirectly found in the kinetic energy budget as enhanced energy dissipation in the bulk, may account for the persistence of this gradient.

Probability density functions show the existence of extreme vorticity structures, both with and without rotation, pointing at a state of 'hard turbulence' [30]. The temperature has Gaussian statistics [10,50], unlike the nearly exponential statistics in the non-rotating case [47]. This suggests that mixing of temperature variance is indeed enhanced under rotation, as extreme fluctu-

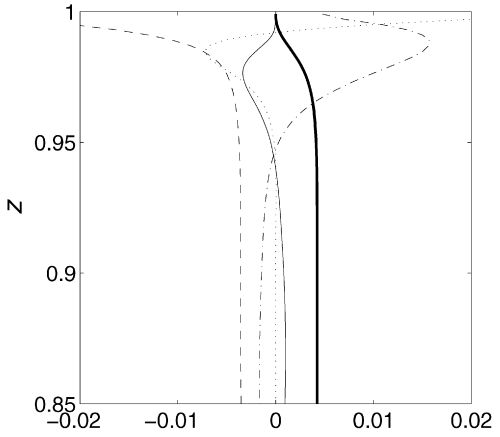

Fig. 15. Kinetic energy budget for $Ra = 2.5 \times 10^7$, $Ro = 1.33$. Line styles are the same as in Fig. 13.

ations are rarer. Vorticity PDFs show exponential shapes at the mid-plane [10]. Near the walls extreme positive skewness is found, indicative of the strong cyclonic vorticity generated there through the Ekman mechanism [10].

The results presented here are useful as a system in which sidewall effects are absent. It is applicable as a model to unbounded convective flows, such as found in the atmosphere. However, comparing these results for horizontally unbounded convection to experiments is rather difficult. As is mentioned in the introduction the sidewalls are found to have considerable impact on the flow-structuring and the heat transfer, even for confined large-aspect-ratio domains. Therefore, we are performing further simulations in a confined cylindrical domain, which are more easily compared with experiments. The first results of these simulations have been reported in [26].

Acknowledgements

R.P.J.K. wishes to thank the Foundation for Fundamental Research on Matter (Stichting voor Fundamenteel Onderzoek der Materie, FOM) for financial support, in the context of the programme “Turbulence and its role in energy conversion processes.” This work was sponsored by the National Computing Facilities Foundation (NCF) for the use of supercomputer facilities, with financial support from the Netherlands Organisation for Scientific Research (NWO).

References

[1] P. Wadhams, J. Holfort, E. Hansen, J.P. Wilkinson, A deep convective chimney in the winter Greenland Sea, Geophys. Res. Lett. 29 (2002) 1434.
[2] J.-C. Gascard, A.J. Watson, M.-J. Messias, K.A. Olsson, T. Johannessen, K. Simonsen, Long-lived vortices as a mode of deep ventilation in the Greenland Sea, Nature (London) 416 (2002) 525–527.
[3] G. Budéus, B. Cisewski, S. Ronski, D. Dietrich, M. Weitere, Structure and effects of a long lived vortex in the Greenland Sea, Geophys. Res. Lett. 31 (2004) L05304.
[4] M.S. Miesch, The coupling of solar convection and rotation, Solar Phys. 192 (2000) 59–89.
[5] F.H. Busse, Convection driven zonal flows and vortices in the major planets, Chaos 4 (1994) 123–134.
[6] E.D. Siggia, High Rayleigh number convection, Annu. Rev. Fluid Mech. 26 (1994) 137–168.
[7] S. Grossmann, D. Lohse, Scaling in thermal convection: a unifying theory, J. Fluid Mech. 407 (2000) 27–56.
[8] L.P. Kadanoff, Turbulent heat flow: structures and scaling, Phys. Today 54 (8) (2001) 34–39.
[9] M. Sprague, K. Julien, E. Knobloch, J. Werne, Numerical simulation of an asymptotically reduced system for rotationally constrained convection, J. Fluid Mech. 551 (2006) 141–174.
[10] K. Julien, S. Legg, J. McWilliams, J. Werne, Rapidly rotating turbulent Rayleigh–Bénard convection, J. Fluid Mech. 322 (1996) 243–273.
[11] R. Verzicco, R. Camussi, Transitional regimes of low-Prandtl thermal convection in a cylindrical cell, Phys. Fluids 9 (1997) 1287–1295.
[12] Lord Rayleigh, On convection currents in a horizontal layer of fluid when the higher temperature is on the underside, Phil. Mag. 32 (1916) 529–546.
[13] S. Chandrasekhar, The instability of a layer of fluid heated from below and subject to Coriolis forces, Proc. R. Soc. Lond. A 217 (1953) 306–327.
[14] S. Chandrasekhar, Hydrodynamic and Hydromagnetic Stability, Oxford University Press, Oxford, 1961.
[15] H.T. Rossby, A study of Bénard convection with and without rotation, J. Fluid Mech. 36 (1969) 309–335.
[16] C. Hunter, N. Riahi, Nonlinear convection in a rotating fluid, J. Fluid Mech. 72 (1975) 433–454.
[17] J.M. Pfotenhauer, P.G.J. Lucas, R.J. Donnelly, Stability and heat transfer of rotating cryogens. Part 2. Effects of rotation on heat-transfer properties of convection in liquid ^{4}He, J. Fluid Mech. 145 (1984) 239–252.
[18] F. Zhong, R.E. Ecke, V. Steinberg, Rotating Rayleigh–Bénard convection: asymmetric modes and vortex states, J. Fluid Mech. 249 (1993) 135–159.
[19] Y. Liu, R.E. Ecke, Heat transport scaling in turbulent Rayleigh–Bénard convection: effects of rotation and Prandtl number, Phys. Rev. Lett. 79 (1997) 2257–2260.
[20] P. Constantin, C. Hallstrom, V. Putkaradze, Heat transport in rotating convection, Physica D 125 (1999) 275–284.
[21] N.K. Vitanov, F.H. Busse, Bounds on the convective heat transport in a rotating layer, Phys. Rev. E 63 (2000) 016303.
[22] R.P.J. Kunnen, H.J.H. Clercx, B.J. Geurts, Heat flux intensification by vortical flow localization in rotating convection, Phys. Rev. E 74 (2006) 056306.
[23] P. Oresta, G. Stringano, R. Verzicco, Transitional regimes and rotation effects in Rayleigh–Bénard convection in a slender cylindrical cell, Eur. J. Mech. B/Fluids 26 (2007) 1–14.
[24] S. Grossmann, D. Lohse, Thermal convection for large Prandtl numbers, Phys. Rev. Lett. 86 (2001) 3316–3319.
[25] S. Grossmann, D. Lohse, Prandtl and Rayleigh number dependence of the Reynolds number in turbulent thermal convection, Phys. Rev. E 66 (2002) 016305.
[26] R.P.J. Kunnen, H.J.H. Clercx, B.J. Geurts, Breakdown of large-scale circulation in turbulent rotating convection, Europhys. Lett. 84 (2008) 24001.
[27] H.P. Greenspan, The Theory of Rotating Fluids, Cambridge University Press, Cambridge, 1968.
[28] S. Sakai, The horizontal scale of rotating convection in the geostrophic regime, J. Fluid Mech. 333 (1997) 85–95.
[29] R.M. Kerr, J.R. Herring, Prandtl number dependence of Nusselt number in direct numerical simulations, J. Fluid Mech. 419 (2000) 325–344.
[30] K. Julien, S. Legg, J. McWilliams, J. Werne, Hard turbulence in rotating Rayleigh–Bénard convection, Phys. Rev. E 53 (1996) R5557–R5560.
[31] R.W.C.P. Verstappen, A.E.P. Veldman, Symmetry-preserving discretization of turbulent flow, J. Comput. Phys. 187 (2003) 343–368.
[32] P. Wesseling, Principles of Computational Fluid Dynamics, Springer, Berlin, 2001.
[33] B. Castaing, G. Gunaratne, F. Heslot, L. Kadanoff, A. Libchaber, S. Thomae, X.-Z. Wu, S. Zaleski, G. Zanetti, Scaling of hard thermal turbulence in Rayleigh–Bénard convection, J. Fluid Mech. 204 (1989) 1–30.
[34] J.J. Niemela, L. Skrbek, K.R. Sreenivasan, R.J. Donnelly, Turbulent convection at very high Rayleigh numbers, Nature (London) 404 (2000) 837–840.
[35] R. Verzicco, R. Camussi, Numerical experiments on strongly turbulent thermal convection in a slender cylindrical cell, J. Fluid Mech. 477 (2003) 19–49.
[36] R.P.J. Kunnen, B.J. Geurts, H.J.H. Clercx, Direct numerical simulation of turbulent rotating Rayleigh–Bénard convection, in: E. Lamballais, R. Friedrich, B.J. Geurts, O. Métais (Eds.), Direct and Large-Eddy Simulation VI, Poitiers, 2006, pp. 233–240.
[37] B.I. Shraiman, E.D. Siggia, Heat transport in high-Rayleigh-number convection, Phys. Rev. A 42 (1990) 3650–3653.
[38] R.M. Kerr, Rayleigh number scaling in numerical convection, J. Fluid Mech. 310 (1996) 139–179.
[39] J.E. Hart, D.R. Ohlsen, On the thermal offset in turbulent rotating convection, Phys. Fluids 11 (1999) 2101–2107.
[40] M.V. Melander, N.J. Zabusky, J.C. McWilliams, Symmetric vortex merger in two dimensions: causes and conditions, J. Fluid Mech. 195 (1988) 303–340.
[41] R.R. Trieling, O.U. Velasco Fuentes, G.J.F. van Heijst, Interaction of two unequal corotating vortices, Phys. Fluids 17 (2005) 087103.
[42] B.M. Boubnov, G.S. Golitsyn, Experimental study of convective structures in rotating fluids, J. Fluid Mech. 167 (1986) 503–531.
[43] F. Zhong, R.E. Ecke, V. Steinberg, Asymmetric modes and the transition to vortex structures in rotating Rayleigh–Bénard convection, Phys. Rev. Lett. 67 (1991) 2473–2476.
[44] P. Vorobieff, R.E. Ecke, Vortex structure in rotating Rayleigh–Bénard convection, Physica D 123 (1998) 153–160.
[45] P. Vorobieff, R.E. Ecke, Turbulent rotating convection: an experimental study, J. Fluid Mech. 458 (2002) 191–218.
[46] J.W. Portegies, R.P.J. Kunnen, G.J.F. van Heijst, J. Molenaar, A model for vortical plumes in rotating convection, Phys. Fluids 20 (2008) 066602.

[47] F. Heslot, B. Castaing, A. Libchaber, Transitions to turbulence in helium gas, Phys. Rev. A 36 (1987) 5870–5873.
[48] T.H. Solomon, J.P. Gollub, Sheared boundary layers in turbulent Rayleigh–Bénard convection, Phys. Rev. Lett. 64 (1990) 2382–2385.
[49] J.A. Glazier, T. Segawa, A. Naert, M. Sano, Evidence against 'ultrahard' thermal turbulence at very high Rayleigh numbers, Nature (London) 398 (1999) 307–310.
[50] J.E. Hart, S. Kittelman, D.R. Ohlsen, Mean flow precession and temperature probability density functions in turbulent rotating convection, Phys. Fluids 14 (2002) 955–962.
[51] S. Balachandar, L. Sirovich, Probability density functions in turbulent convection, Phys. Fluids A 3 (1991) 919–927.
[52] J.W. Deardorff, G.E. Willis, Investigation of turbulent thermal convection between horizontal plates, J. Fluid Mech. 28 (1967) 675–704.
[53] C.-H. Moeng, R. Rotunno, Vertical-velocity skewness in the buoyancy-driven boundary layer, J. Atmos. Sci. 47 (1990) 1149–1162.
[54] R.M. Kerr, Energy budget in Rayleigh–Bénard convection, Phys. Rev. Lett. 87 (2001) 244502.
[55] M. van Reeuwijk, H.J.J. Jonker, K. Hanjalić, Identification of the wind in Rayleigh–Bénard convection, Phys. Fluids 17 (2005) 051704.
[56] M. van Reeuwijk, H.J.J. Jonker, K. Hanjalić, Wind and boundary layers in Rayleigh–Bénard convection. I. Analysis and modeling, Phys. Rev. E 77 (2008) 036311.
[57] M. van Reeuwijk, H.J.J. Jonker, K. Hanjalić, Wind and boundary layers in Rayleigh–Bénard convection. II. Boundary layer character and scaling, Phys. Rev. E 77 (2008) 036312.
[58] N.N. Mansour, J. Kim, P. Moin, Reynolds-stress and dissipation-rate budgets in a turbulent channel flow, J. Fluid Mech. 194 (1988) 15–44.